Atmos. Meas. Tech. Discuss., https://doi.org/10.5194/amt-2018-327
Manuscript under review for journal Atmos. Meas. Tech.
Discussion started: 8 January 2019
© Author(s) 2019. CC BY 4.0 License.

Atmospheric Measurement Techniques Discussions

A geometry-dependent surface Lambertian-equivalent reflectivity product at 466 nm for UV/Vis retrievals: Part I. Evaluation over land surfaces using measurements from OMI

Wenhan Qin[1], Zachary Fasnacht[1], David Haffner[1], Alexander Vasilkov[1], Joanna Joiner[2], Nickolay Krotkov[2], Brad Fisher[1], and Robert Spurr[3]

[1]Science Systems and Applications Inc., Lanham, MD, USA
[2]NASA Goddard Space Flight Center, Greenbelt, MD, USA
[3]Rt Solutions Inc., Cambridge, MA, USA

Correspondence to: W. Qin (wenhan.qin@ssaihq.com)

Abstract. The anisotropy of the Earth's surface reflection has implications for satellite-based retrieval algorithms that utilize climatological surface reflectivity databases that do not depend upon the observation geometry. This is the case for most of the current ultraviolet and visible (UV/Vis) cloud, aerosol, and trace-gas algorithms. The illumination-observation dependence of surface reflection is described by the bidirectional reflectance distribution function (BRDF). To account for the BRDF effect, we use the concept of geometry-dependent surface Lambertian-equivalent reflectivity (GLER), which is derived from the top-of-atmosphere (TOA) radiance computed with Rayleigh scattering and surface BRDF for the exact geometry of a satellite-based pixel. We present details on the implementation of land and water surface BRDF models. We evaluate our GLER product over land surfaces using observed and computed sun-normalized radiances at 466 nm. The input surface BRDF parameters for computing TOA radiance are derived from MODerate-resolution Imaging Spectroradiometer (MODIS) satellite observations. The observed TOA radiance for comparison is from the Ozone Monitoring Instrument (OMI). The comparison shows good agreement between observed and calculated OMI radiances in typical geographical regions, with correlation coefficients greater than 0.9 for a majority of the selected regions in the year of 2006. Seasonal variations of clear-sky OMI radiances (i.e., with minimum clouds and aerosols) closely follow those computed using MODIS-derived GLER over land. GLER also captures the cross-track dependence of OMI radiances, although the observations are slightly higher than those computed using GLER presumably owing to residual cloud and aerosol (non-absorbing) contamination, particularly over dark surfaces (heavily vegetated regions such as mixed forest, croplands and grasslands). The standard OMI climatological surface reflectivity database predicts higher radiances than GLER and OMI ob-

Atmos. Meas. Tech. Discuss., https://doi.org/10.5194/amt-2018-327
Manuscript under review for journal Atmos. Meas. Tech.
Discussion started: 8 January 2019
© Author(s) 2019. CC BY 4.0 License.

Atmospheric Measurement Techniques Discussions

servations with different seasonal variations and cross-track dependence over most of the selected regions. Overall, our evaluation demonstrates that the GLER product adequately accounts for surface BRDF effects while at the same time simplifies the surface BRDF implementation within the existing OMI retrieval infrastructure; use of our GLER product requires changes only to the input surface reflectivity database.

1 Introduction

It is well-known that reflection of the incident sunlight by the Earth's surface is generally anisotropic in the optical wavelength range (Rencz and Ryerson, 1999). Rough surfaces (vegetated landscapes, urban and built-up, bare soils, etc) usually exhibit marked backward scattering, whereas smooth surfaces (e.g., water, snow/ice) tend to have a strong forward scattering peak (specular reflection). Two well-known phenomena related to surface reflection anisotropy are the hot-spot effect over land and the sunglint over ocean. The hot-spot effect occurs when the viewing direction coincides with the illumination direction, such that all shadows are invisible. This results in a reflectance peak in backward scattering directions (e.g., Qin et al., 1996). Sunglint, however, is a peak in forward scattering caused by Fresnel reflection over a smooth surface such as calm water, when sunlight reflects off the surface at the same angle that the surface is viewed (e.g., Kay et al., 2009).

The dependence of surface reflection on illumination and observation directions is mathematically described by the bidirectional reflectance distribution function (BRDF), an intrinsic property of the surface (Nicodemus, 1965; Martonchik et al., 2000; Schaepman-Strub et al., 2006). Since BRDF is defined in terms of differential solid angles, in theory it cannot be measured (Nicodemus, 1977). Therefore, another quantity which can be retrieved from remote sensing data, the bidirectional reflectance factor (BRF), has been widely used ever since. BRF is defined as the ratio of the reflected radiance from the surface to that from a perfect Lambertian surface under the same geometry (illumination and observation) and ambient conditions. Since an ideal diffuse surface reflects the same radiance in all viewing directions, the BRDF for a Lambertian surface is $1/\pi$. Because of this, the BRF for any surface is equal to its BRDF times π. However, unlike the BRDF, BRF is a unitless quantity.

The effect of surface anisotropy on satellite-observed radiances propagates through the atmosphere and may produce complex errors. The influence of surface anisotropy on the top of the atmosphere (TOA) radiance increases with wavelength for a Rayleigh atmosphere (no aerosols or clouds) because atmospheric transmittance increases with wavelength in the ultraviolet and visible (UV/Vis) spectral regions. Under natural conditions for Earth observing, the incident irradiance comprises a direct component (non-scattered radiation) and a diffuse component scattered by the atmosphere (gases, aerosols, and clouds) and by the surroundings of the observed surface (e.g., topography). The magnitude and spectral distribution of the diffuse irradiance depends on atmospheric

Atmos. Meas. Tech. Discuss., https://doi.org/10.5194/amt-2018-327
Manuscript under review for journal Atmos. Meas. Tech.
Discussion started: 8 January 2019
© Author(s) 2019. CC BY 4.0 License.

Atmospheric Measurement Techniques Discussions

conditions. Over a clear sky, the diffuse component originates from Rayleigh scattered sunlight that follows a λ^{-4} dependence, where λ is wavelength. As a result, the surface anisotropy impact on TOA radiance is very strong for visible or longer wavelengths simply because the atmosphere is much more transparent at these wavelengths.

The surface reflectance anisotropy has implications for UV/Vis satellite retrievals of aerosols, clouds, and trace gases such as nitrogen dioxide (NO_2). Currently, most satellite-based UV/Vis algorithms (e.g., Krotkov et al., 2017) use surface reflectivity climatologies, typically gridded monthly Lambertian-equivalent reflectivities (LERs) that have been derived from satellite observations (e.g., Herman and Celarier, 1997; Koelemeijer et al., 2001; Kleipool et al., 2008). These climatologies are typically constructed by statistically analyzing multiple years of observations that have various Sun-viewing geometries. In order to minimize cloud contamination, they may be based on a lower percentile or the mode of the LER histogram depending on surface type (Kleipool et al., 2008). As pointed out recently by Lorente et al. (2018), such climatologies tend to pick up the lowest values among the measurements of a scene, typically corresponding with forward (backward) scattering geometries over land (water).

An example of the impact of LER climatologies on cloud fraction retrievals is the presence of considerable cross-track biases. This has been shown for satellite retrievals in the O_2-A band (Wang et al., 2008) as well as for the 477 nm O_2-O_2 band (Veefkind et al., 2016). This happens because the LER climatologies tend to underestimate the actual LER in the backward scattering directions (usually the west side of the scan line) over land, and the retrieval compensates for this by overestimating cloud fractions in order to match the observed TOA reflectance. Over ocean, such overestimation of cloud fraction would occur in the forward scattering directions (east side).

To account for surface anisotropy in existing cloud and trace gas algorithms that make use of the LER, we implement the concept of geometry-dependent LER (GLER), which was introduced by Vasilkov et al. (2017). GLER is derived from simulated TOA radiance of a Rayleigh atmosphere over a non-Lambertian surface for the specific geometry of a satellite pixel. Here "geometry-dependent" is emphasized to distinguish the GLER product (which considers the angular dependence of surface reflection) from other LER-related products or climatologies that have no dependence on sun/satellite geometries. Our GLER approach does not require major changes to existing trace gas and cloud algorithms that rely on an estimate of LER (Vasilkov et al., 2017); the main revision to the algorithms requires replacement of the existing static LER climatologies with GLERs calculated for specific fields-of-view (FOVs) and Sun-satellite geometries. GLERs can be applied to any satellite retrieval algorithm that uses LERs.

The main goal of this paper is to evaluate our GLER product over land surfaces using visible measurements from the satellite-borne Ozone Monitoring Instrument (OMI). In the current version, the GLER is based on BRDF parameters derived from MODerate-resolution Imaging Spectroradiometer (MODIS) satellite observations over land; we plan to cover the ocean results in a separate paper. We

Atmos. Meas. Tech. Discuss., https://doi.org/10.5194/amt-2018-327
Manuscript under review for journal Atmos. Meas. Tech.
Discussion started: 8 January 2019
© Author(s) 2019. CC BY 4.0 License.

Atmospheric Measurement Techniques Discussions

also provide additional details on the GLER methodology, including the determination of the product components and key input model parameters. Specifically, models used for radiative transfer (RT) calculations for both atmosphere and surfaces are introduced in Section 2. We compare OMI-measured and simulated TOA radiances and LERs over typical geographical regions as a function of cross-track position, season, and year in Section 3. Discussion and conclusions are provided in the final two sections.

2 Data and Methods

In this section, we describe data sets and methodologies used to estimate each component of GLER. The implementation and validation process is summarized in Figure 1. The focus of this paper is on evaluating the derived GLER over land surfaces (pixel land fraction ≥ 0.99). However, for completeness, details on ocean models are given in Appendix A.

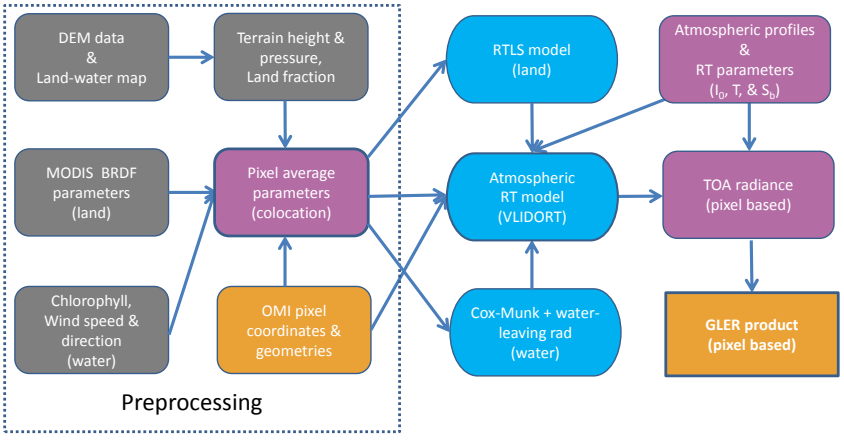

Fig. 1: Flowchart of the GLER processes. Different colors stand for different data types/sources: grey for ancillary data for both land and water, purple for preprocessed input parameters or atmospheric input parameters, gold for sensor-dependent pixel-related inputs/ouput, and finally, blue ovals for the physical models used. All input data are represented by the rounded rectangles and output product is shown in the box rectangle. DEM denotes digital elevation model. RTLS denotes the Ross-Thick/Li-Sparse Reciprocal functions (see section 2.1 below for details). Also see Eq. 2 for definitions of I_0, T and S_b and Appendix A for models used over water.

Atmos. Meas. Tech. Discuss., https://doi.org/10.5194/amt-2018-327
Manuscript under review for journal Atmos. Meas. Tech.
Discussion started: 8 January 2019
© Author(s) 2019. CC BY 4.0 License.

2.1 Kernel-driven BRDF and land type products for land surfaces from MODIS

MODIS is a cross-track scanning radiometer and has 36 spectral bands ranging in wavelength from 0.4 μm to 14.4 μm. Two bands (1 and 2) have a nominal resolution of 250 m at nadir, with five bands (3 to 7) at 500 m, and the remaining 29 bands at 1 km. MODIS views the entire Earth surface approximately daily via a two-side scan mirror that provides a swath of 2330 km cross track by 10 km along track (at nadir) each scan. The MODIS instruments are operated onboard the National Aeronautics and Space Administration (NASA) Aqua and Terra satellites, which have 16-day repeat cycles and provide measurements on a global basis every 1-2 days. MODIS data are used to study the oceans, atmosphere and land (Justice et al., 1998).

To compute GLERs, we use Collection 5 MODIS BRDF/Albedo Product MCD43 for land surfaces (Sun et al., 2017; Schaaf et al., 2002, 2011). This product uses the atmospheric corrected surface reflectance data (MOD09) from MODIS instruments on both Aqua and Terra satellites (Vermote and Kotchenova, 2008). Atmospheric correction has been carried out based on the Second Simulation of a Satellite Signal in the Solar Spectrum, Vector (6SV) radiative transfer code (Vermote et al., 1997; Kotchenova and Vermote, 2007; Vermote and Kotchenova, 2008). The overall accuracy of surface reflectance varies with band and aerosol optical thickness (AOT) (Vermote et al., 2002). Under clear atmospheric conditions at band 3 (470 nm), the accuracy is about 0.005 in reflectance unit as shown in Table 2 of Vermote and Kotchenova (2008). The relative error due to the Lambertian assumption on surface reflectance does not exceed 0.8% in the inter-model comparison (Kotchenova and Vermote, 2007), but could be much higher (e.g., 3-12% in the green band) when comparing to multiangular field measurements (Franch et al., 2013).

Since the morning overpass (Terra) and afternoon overpass (Aqua) view the same location with different Sun-viewing geometries, use of data from both satellites would double the angular samples during the 16-day repeat cycle and reduce the uncertainty and random noise amplification of anisotropy retrievals (Schaaf et al., 2011). The MCD43 product has been extensively validated on different platforms at different scales across different landscapes. Most of the validation efforts has focused on albedo validation of the product (Salomon et al., 2006; Knobelspiesse et al., 2008; Liu et al., 2009; Roman et al., 2009; Wang et al., 2010). Two particular comparisons with airborne multiangle observations, the Cloud Absorption Radiometer (CAR) measurements (Roman et al., 2013) and the Airborne Hyperspectral Scanner (AHS) data (Sobrino et al., 2013), have demonstrated a very good agreement with the airborne images, and MODIS-derived estimates met the accuracy requirements established for the high-quality MODIS operational product when solar zenith angle (SZA) is less than 70°.

The kernel-driven BRDF model used in the MCD43 BRDF/Albedo algorithm is known as the Ross-Thick/Li-Sparse Reciprocal (RTLS). RTLS consists of a linear combination of the weighted sum of an isotropic parameter and two kernels of viewing and illumination geometry (Roujean et al., 1992). The Ross-Thick kernel is derived from radiative transfer models (Ross, 1981) for volume

Atmos. Meas. Tech. Discuss., https://doi.org/10.5194/amt-2018-327
Manuscript under review for journal Atmos. Meas. Tech.
Discussion started: 8 January 2019
© Author(s) 2019. CC BY 4.0 License.

Atmospheric Measurement Techniques Discussions

scattering within a dense vegetation canopy, and the Li-Sparse Reciprocal kernel is based on surface scattering and geometric shadow-casting with mutual shadowing theory (Li and Strahler, 1992).

The mathematical expression for the kernel-driven RTLS to estimate surface BRF is as follows:

$$\mathrm{BRF}(\lambda,\theta,\theta_0,\phi) = f_{\mathrm{iso}}(\lambda) + f_{\mathrm{vol}}(\lambda)k_{\mathrm{vol}}(\theta,\theta_0,\phi) + f_{\mathrm{geo}}(\lambda)k_{\mathrm{geo}}(\theta,\theta_0,\phi), \quad (1)$$

where θ is the viewing zenith angle (VZA), θ_0 the solar zenith angle (SZA), and ϕ the relative azimuth angle (RAA). k_{vol} and k_{geo} are the Ross-Thick and Li-Sparse Reciprocal kernels; f_{iso}, f_{vol} and f_{geo} are the kernel weights (also called kernel coefficients or BRDF parameters) derived every 8 days by inverting the model against MODIS multi-angular observations (cloud-cleared, atmospherically corrected surface reflectances) collected for each location within a 16-day period. MCD43 provides three kernel coefficients (f_{iso}, f_{vol}, and f_{geo} in Eq. 1) for 7 MODIS bands for snow-free land and permanent snow and ice cover every 8 days. The static land-water flag that is provided with MCD43 has same spatial resolution (30″) with eight surface categories.

Global characterization of BRDF from satellite measurements for surfaces covered by snow and ice is an area of active research. Though recent improvements in the MODIS Collection 6 MCD43 BRDF data (Wang et al., 2018) may enable the use of the MCD43 data for seasonal and variable short-term snow cover in GLER product, the first version of the GLER product uses the gap filled (GF) Collection 5 product (MCD43GF) which is intended to provide BRDF parameters using the RTLS model for land surfaces free of seasonal snow and those covered by permanent snow or ice. Other snow and ice BRDF models also exist, and, in fact, the calibration of the OMI instrument, described in section 2.2, is based partly on an alternate model to describe reflectance from Antarctic ice (Jaross and Warner, 2008). Because validation of snow and ice reflectances is challenging and involves different issues than those of snow-free land, we plan to carefully evaluate the GLER product over snow and ice separately in a follow-on study using various sources of BRDF information. Until that time, the GLER product over snow and ice should be considered less mature than the BRDF over snow and ice free land, whether the snow and ice are permanent (using MCD43GF), or seasonal (using OMI-derived LER) as described in section 4.

To obtain kernel coefficients for a given OMI pixel, the collocated MCD43GF points within an OMI pixel FOV are averaged. The pixel land fraction is estimated by converting the eight surface category map into a binary land-water mask, i.e., merging all shorelines and ephemeral water into the land category and classifying all other water sub-categories simply as water. The areal fraction of land (or water) for each OMI pixel is then computed as the statistics of the binary categories. Typical results are shown in Figure 2. Our approach of estimating the land area fraction provides for more accurate calculation of TOA radiances in mixed pixels (see Eq. 3) as compared with the use of the eight surface category flags in the OMI level 1b data set. Accurate estimation of pixel land fraction is also very important because BRDF models for land and water surfaces are quite different (strong backward scattering over land vs strong forward scattering over water) with different wavelength

Atmos. Meas. Tech. Discuss., https://doi.org/10.5194/amt-2018-327
Manuscript under review for journal Atmos. Meas. Tech.
Discussion started: 8 January 2019
© Author(s) 2019. CC BY 4.0 License.

Atmospheric Measurement Techniques Discussions

dependence. In contrast with previous studies (e.g., Zhou et al., 2010), we apply the ocean models described in Appendix A to coastal zones and inland waters instead of using MODIS data, because the MODIS kernel model is not applicable for water surfaces.

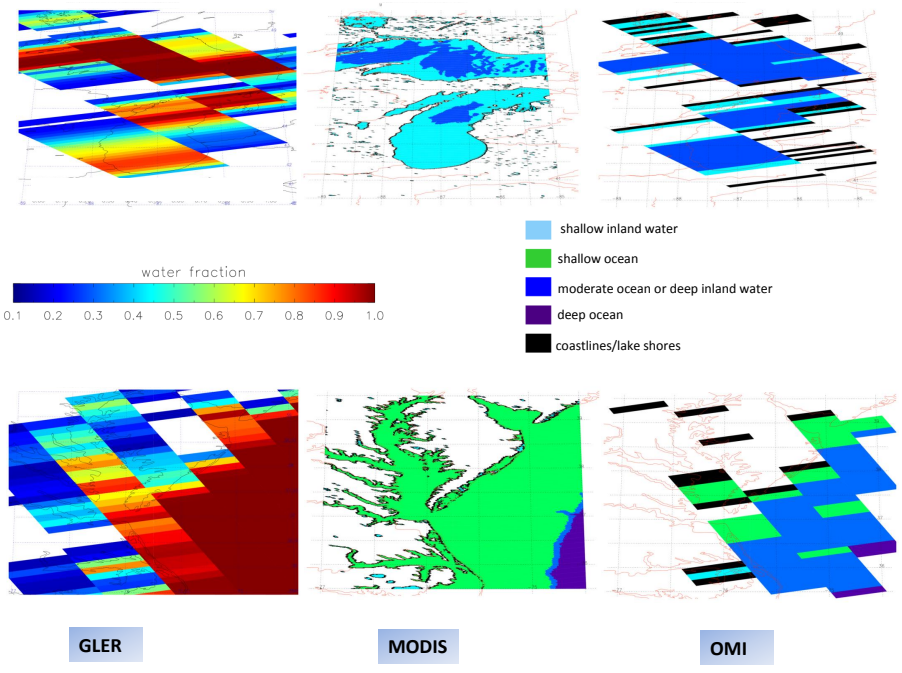

Fig. 2: Pixel water fractions (color bar) estimated in GLER (left), MODIS 30″ land-water map (middle), and OMI L1b pixel land-water category (right). The five-color legend denotes surface categories defined in the original MODIS or OMI L1b data. Top panel: region of Lakes Superior and Michigan; Bottom panel: Chesapeake Bay.

The above kernel coefficients depend on wavelength. For the present study we selected MODIS band 3, the shortest wavelength in the MCD43GF product, with a center wavelength of 470 nm (ranging from 459 to 479 nm) to represent 466 nm, which is the wavelength used in our cloud algorithm to retrieve effective cloud fraction (ECF) (Yang et al., 2015). Observations at this wavelength are relatively free of atmospheric rotational-Raman scattering (RRS) and trace gas absorption.

2.2 OMI data and selection criteria

OMI, launched onboard the NASA Aura satellite in July 2004, is a Dutch-Finnish hyper-spectral passive imager measuring in the 270-500 nm wavelength range with two CCD detectors (UV and Vis). It was designed to provide information about trace-gases, such as O_3, NO_2, SO_2, HCHO, as

Atmos. Meas. Tech. Discuss., https://doi.org/10.5194/amt-2018-327
Manuscript under review for journal Atmos. Meas. Tech.
Discussion started: 8 January 2019
© Author(s) 2019. CC BY 4.0 License.

Atmospheric Measurement Techniques Discussions

well as absorbing aerosols. OMI has an instantaneous FOV of 0.8° in the flight direction (along-track) and 115° in the swath direction (cross-track), which yields an overall ground coverage of about 13 km by 2600 km at an altitude of 700 km. OMI measurements nominally provide daily global coverage with a 13 km × 24 km resolution in the nadir position.

OMI collection 3 data are used in this study. Specifically, we use LERs retrieved from TOA reflectances at 466 nm that are computed by normalizing the OMI radiances to the OMI day-1 solar irradiance spectrum. The GLER product is designed to characterize the magnitude and the angular variability of the Earth's surface reflectance under a Rayleigh atmosphere, so in the context of GLER product validation, absolute radiometric response and consistency across the measurement swath are the two most critical aspects of instrument calibration to consider. For this study we ignore spectral dependence in the calibration, because our focus is strictly on the 466 nm channel. Spectral calibration will be important for validation of future versions of the GLER product that are planned to report data at several other wavelengths.

The OMI calibration has been detailed in previous work. Dobber et al. (2008) estimated that the uncertainty in viewing angle dependence of OMI collection 3 sun-normalized radiances is less than 2%. Their estimate follows the application of calibration adjustments based on the evaluation of TOA measurements over a target region of Antarctic ice, using a surface model that accounts for non-Lambertian effects in a radiative transfer model of the atmosphere as described by Jaross and Warner (2008). In that work, the authors used the same technique to establish the absolute radiometric calibration of OMI at nadir within an estimated model uncertainty of 1%. Schenkeveld et al. (2017) evaluated long-term changes in the absolute radiometric response of the OMI instrument and estimated degradation of approximately 1-1.5% over the lifetime of the mission in the wavelength region used in this study.

Since only clear sky measurements are used for our comparison, we apply the UV aerosol index (AI) from OMAERUV product (Torres et al., 2007) to detect and screen out absorbing aerosol contaminated OMI measurements. This aerosol index is defined as the ratio of radiances measured at 354 and 388 nm compared to the ratio calculated for a pure Rayleigh-scattering atmosphere. It is sensitive to the presence of absorbing aerosols that reduce LER retrieved from OMI data. To screen out cloud contaminated pixels in the OMI measurements, we use ECF (effective cloud fraction) from the oxygen dimer ($O_2 - O_2$) cloud product described in Vasilkov et al. (2018). The criteria we chose for data screening are $|\mathrm{AI}| < 1.0$ and $\mathrm{ECF} < 0.02$. We found that more stringent criteria than these removed too much data from the analysis, and that relaxation above these thresholds began to introduce cloud and aerosol contamination that noticeably degraded the results.

2.3 Ancillary data sets

In order to produce the pixel-level GLER product, we need first to collocate and average ancillary data that have different spatial resolutions over the OMI FOV for the physical models that we

Atmos. Meas. Tech. Discuss., https://doi.org/10.5194/amt-2018-327
Manuscript under review for journal Atmos. Meas. Tech.
Discussion started: 8 January 2019
© Author(s) 2019. CC BY 4.0 License.

Atmospheric Measurement Techniques Discussions

use. Table 1 summarizes the ancillary data used in terrestrial GLER production along with their spatio-temporal resolutions. This includes digital elevation model (DEM) data (ETOPO2v2) from the National Oceanic and Atmospheric Administration (NOAA). The ancillary data with higher spatial resolution than OMI are first colocated with the OMI pixel using the so-called point-in-polygon methodology described by Haines (1994) and applied by Fisher et al. (2014) in the development of a merged OMI-MODIS cloud product. An example to use this method to colocate the high resolution MODIS BRDF product (MCD43GF) is shown in Figure 3. Actually, this colocation method can be applied to any kind of satellite pixel shapes. An OMI pixel is defined with respect to the

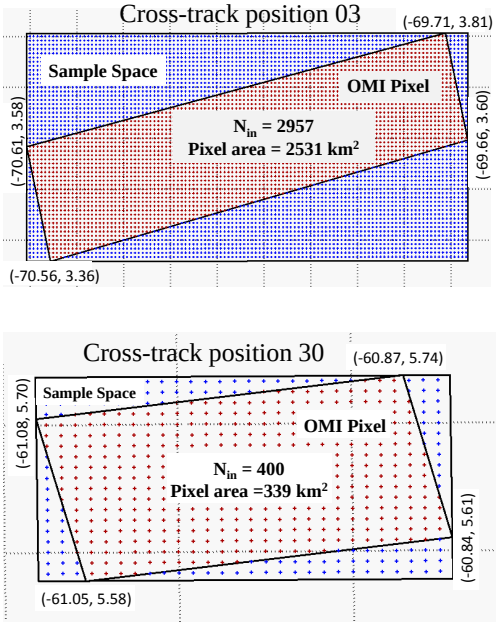

Fig. 3: An illustration of colocating the high resolution MODIS BRDF data with an OMI pixel FOV. Sample space is defined as the MODIS data space that encloses the entire OMI pixel polygon. N_{in} is the number of MODOS data points within the OMI pixel (red dots). Numbers at each pixel corner indicate its geolocation (longitude, latitude). Two pixels are selected: cross-track position 03 (near the edge of swath) and cross-track position 30 (near nadir) for orbit 12399 with along-track position 1000.

polygon formed by the four OMI-pixel corner points, as described in the OMPIXCOR data product (see https://disc.gsfc.nasa.gov/datacollection/OMPIXCOR_003.html for more information). OMPIXCOR provides two sets of coordinates 1) Non-overlapping and 2) Overlapping coordinates. We used the Vis channel overlapping coordinates, corresponding to 75% of the energy in the along-track

Atmos. Meas. Tech. Discuss., https://doi.org/10.5194/amt-2018-327
Manuscript under review for journal Atmos. Meas. Tech.
Discussion started: 8 January 2019
© Author(s) 2019. CC BY 4.0 License.

field-of-view, as they are considered more accurate for scientific analysis than the non-overlapping coordinates that are provided mainly for mapping purposes. Additional details regarding the collocation and averaging of ancillary data sets are given in Appendix B.

Table 1: Spatial and temporal resolutions of ancillary data used for land GLER calculation

Name	Source	Spatial	Temporal
DEM	ETOPO2v2/NOAA	$2'$	N/A
Land-water flag	MODIS	$30''$	N/A
Land BRDF parameters	MCD43GF/MODIS	$30''$	8 days

2.4 GLER computation

Given all necessary input parameters, TOA radiances (I_{comp}) are computed with the Vector Linearized Discrete Ordinate Radiative Transfer (VLIDORT) model. VLIDORT is a multiple scattering radiative transfer model that can simulate Stokes 4-vectors at any level in the atmosphere and for any scattering geometry with a Lambertian or non-Lambertian underlying surface (Spurr, 2006). VLIDORT has the ability to simulate attenuation of solar and line-of-sight paths in a spherical atmosphere. In this study, we consider the sphericity correction for both incoming solar and outgoing viewing directions based on a regular pseudo-spherical geometry calculation. This is important for large solar and viewing zenith angles. We also consider polarization using the vector mode, because neglect of polarization can lead to considerable errors for modeling backscattered spectra in the UV/Vis wavelength range. The MODIS semi-empirical kernel-driven BRDF function is selected from the group of analytical BRDF models available in the VLIDORT BRDF supplement. This surface BRDF supplement is a separate module from the VLIDORT main program and can be upgraded by adding new analytical BRDF models as needed.

Then GLER (or simply R) is derived by inverting

$$I_{\text{comp}}(\lambda,\theta,\theta_0,\phi,P_s,\text{BRF}_s) = I_0(\lambda,\theta,\theta_0,\phi,P_s) + \frac{RT(\lambda,\theta,\theta_0,P_s)}{1-RS_b(\lambda,P_s)}, \quad (2)$$

where P_s is the pressure at the reflecting surface, I_0 is the path scattering radiance by the atmosphere, calculated as the TOA radiance for a black surface, T is the transmitted radiance, i.e., incident total (direct + diffuse) irradiance multiplying by transmittance from TOA to the reflecting surface along the incoming solar beam as well as that from the surface to TOA along the satellite view direction, and S_b is the diffuse flux reflectivity of the atmosphere, i.e., the fraction of upward radiance from the surface scattered back to the surface by the atmosphere (Dave, 1978). All angles are defined as in Eq. 1. The input surface BRF (i.e., BRF_s) to VLIDORT is simulated either with Eq. 1 over land or with models described in Appendix A over water. To speed up computations, we created lookup tables of the quantities I_0, T and S_b for different Sun-viewing geometries and for a number

Atmos. Meas. Tech. Discuss., https://doi.org/10.5194/amt-2018-327
Manuscript under review for journal Atmos. Meas. Tech.
Discussion started: 8 January 2019
© Author(s) 2019. CC BY 4.0 License.

Atmospheric Measurement Techniques Discussions

of surface pressure levels (see Appendix C for details). Note that Eq. 2 can also be used to derive LER directly from satellite observations by simply replacing the computed TOA radiance ($I_{\rm comp}$) with observed TOA radiance ($I_{\rm obs}$). This approach is used in Section 3, where we compute and compare OMI-derived LER to VLIDORT-simulated GLER for validation.

To calculate TOA radiance with VLIDORT on a pixel basis, we construct dynamical atmospheric optical property profiles using the surface (terrain) pressure, temperature and their profiles pixel by pixel. The pressure profile is then generated following Lagrangian control volume (LCV) coordinate system starting from the surface pressure (see discussion in Appendix B). The temperature profile is based on the Global Modeling Initiative (GMI, see Rienecker et al. (2011)) monthly climatological temperature profiles. Finally, we calculate the layer total optical thickness and single scattering albedo following Bodhaine et al. (1999) for Rayleigh cross-section calculation. Compared with the static profiles used previously (e.g., Vasilkov et al., 2017), these dynamic atmospheric profiles better represent the actual Rayleigh atmosphere above the pixel and result in a more accurate TOA radiance simulation.

For uniform surface pixels (either 100% land or water), we calculate TOA radiance by coupling the surface anisotropy models specified in Section 2.1 (for land) or Appendix A (for water) with VLIDORT. For heterogeneous surface pixels (i.e., mixed with land and water), the TOA radiance is estimated using an area-weighted radiance for uniform land ($I_{\rm land}$) and water ($I_{\rm water}$) contributions within an OMI FOV, i.e., replacing $I_{\rm comp}$ in Eq. 2 with

$$I^{\rm TOA}_{\rm comp} = f_L I^{\rm TOA}_{\rm land} + (1 - f_L) I^{\rm TOA}_{\rm water}, \tag{3}$$

where f_L is the pixel land fraction, estimated as described in Section 2.1. Figure 4 shows examples of $I^{\rm TOA}_{\rm land}$, $I^{\rm TOA}_{\rm water}$ and $I^{\rm TOA}_{\rm comp}$.

It should be noted that aerosols are not included in the computation of the GLER. Scattering by aerosols in the atmosphere reduces the BRDF effects (Noguchi et al., 2014). Therefore, the use of the GLER may result in overestimation of the BRDF effects in the presence of aerosol and thin clouds. Our use of a retrieved effective cloud fraction (that implicitly accounts for the effects of non-absorbing aerosol) will help to alleviate this problem. We plan to examine aerosol effects on GLER in a future work.

3 Results

First, we examine the overall performance of GLER by comparison with the OMI-derived LER. OMI-derived LER (i.e., R in Eq. 2) is calculated by solving this equation with OMI-measured TOA radiance as input for $I_{\rm comp}$ and other quantities (I_0, T and S_b) from lookup tables, as described in Section 2.4, for a given pixel's Sun-viewing geometry and surface pressure.

Then we carry out an in-depth evaluation over nine typical landscapes (see Table 2 and Figure 5) covering seasonal, interannual, and cross-track variations.

Atmos. Meas. Tech. Discuss., https://doi.org/10.5194/amt-2018-327
Manuscript under review for journal Atmos. Meas. Tech.
Discussion started: 8 January 2019
© Author(s) 2019. CC BY 4.0 License.

Atmospheric Measurement Techniques Discussions

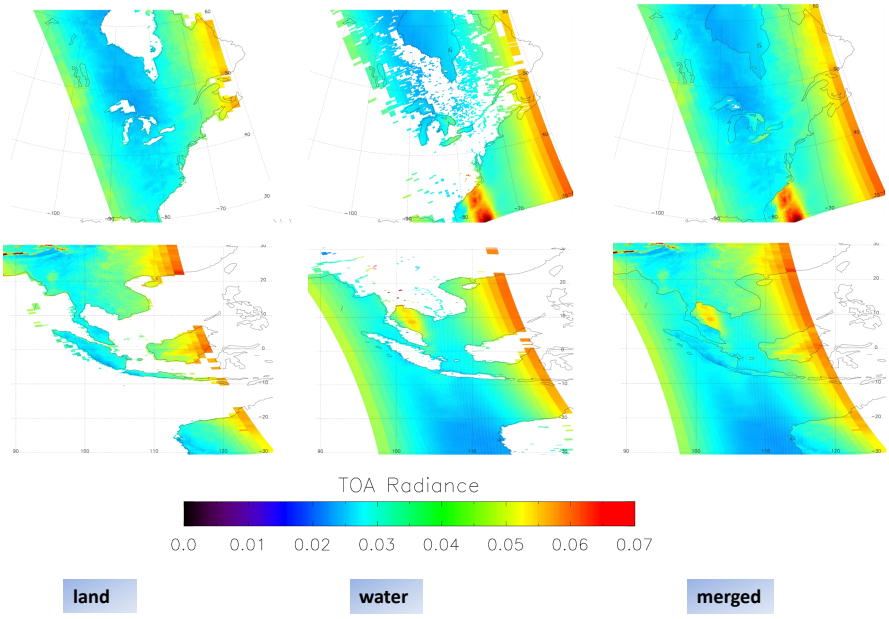

Fig. 4: Pixel-based simulated TOA radiance over land (left) when the pixel land fraction is larger than 5%, water (middle) when the pixel water fraction is larger than 5%, and the merged scene using Eq. 3 (right). Top panel: North America; Bottom panel: SE Asia.

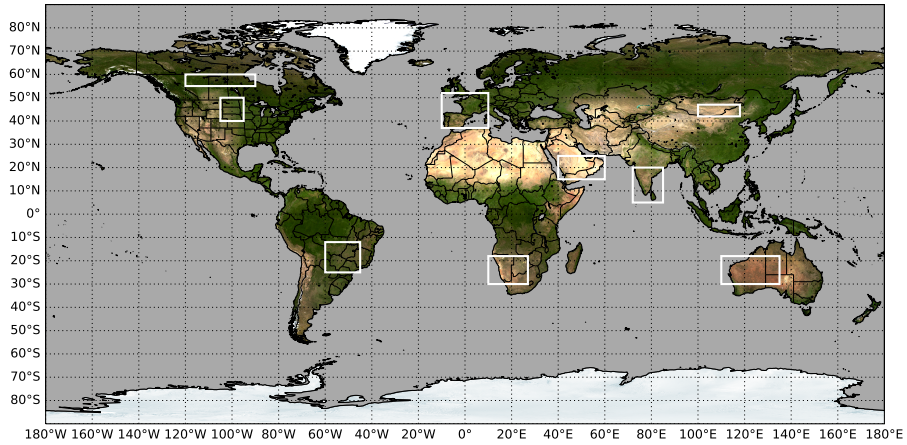

Fig. 5: Locations of selected geographical regions as specified in Table 2

.

3.1 Overall performance

Figures 6–8 show comparisons of GLER with clear-sky OMI-derived LER at 466 nm across various geographical regions for different seasons in 2006. The absolute LER varies between regions; for

Atmos. Meas. Tech. Discuss., https://doi.org/10.5194/amt-2018-327
Manuscript under review for journal Atmos. Meas. Tech.
Discussion started: 8 January 2019
© Author(s) 2019. CC BY 4.0 License.

Atmospheric Measurement Techniques Discussions

Table 2: Selected geographical regions for analysis

Region	Land Type	Longitude Range	Latitude Range
central Canada	Boreal Forest	120W-90W	55N-60N
central United States	Cropland/Grassland	105W-95W	40N-50N
southern Brazil	Cropland	60W-45W	25S-12S
Spain/France	Cropland/Forest	10W-10E	37N-52N
Arabian Desert	Barren	40E-60E	15N-25N
southern Africa	Open Shrubland	10E-27E	30S-18S
southern India	Crop Mosaic	72E-85E	5N-20N
Mongolia	Barren/Desert	100E-118E	42N-47N
western Australia	Open Shrubland	110E-135E	30S-18S

example, forested regions have lower LER, and deserts have higher LER. Overall, the OMI-derived LER is generally higher compared with the calculated GLER, as the majority of the scatterplots have negative y-intercepts. There are several possible reasons for the differences, such as some background non-absorbing aerosols that slightly increase the OMI-derived reflectivity and small calibration differences between MODIS and the OMI instruments.

Despite this small bias, we note that $r^2 > 0.8$ for most regions, with the poorest agreement in darker regions such as southern Brazil and central Canada. The brighter regions such as Mongolia and the Arabian desert exhibit excellent agreement with $r^2 > 0.9$. It is possible that in these regions the enhanced brightness of the surface minimizes the impact of aerosols and clouds. The comparison has the largest seasonal variation in regions where vegetation changes the most through the year, such as in southern Brazil. The desert regions such as the Arabian Desert show no change with season. In the Mongolia region there is a portion of data with GLER greater than OMI derived LER during the winter months; it is possible that this is due to snow contamination in the MODIS BRDF data (Riggs et al., 2016).

3.2 Seasonal variations

While surface BRDF does not change on a day-to-day basis, there is variability in the BRDF between seasons due to land cover changes throughout the year. Since the MODIS BRDF parameters are calculated every 8 days, they capture the changes in BRDF from season to season over various land cover types. Figure 9 shows the seasonal variability of LER from model simulations and OMI-derived LER for various land cover types in 2006 for cloud and aerosol free pixels. Comparisons of OMI reflectivity data with GLERs in the central Canada region are excluded due to the presence of seasonal snow cover, while in the southern India region, missing data occur due to persistent cloud cover during the monsoon season.

Throughout the year, both GLER and OMI-derived LER vary as much as 0.03-0.04 at 466 nm.

Atmos. Meas. Tech. Discuss., https://doi.org/10.5194/amt-2018-327
Manuscript under review for journal Atmos. Meas. Tech.
Discussion started: 8 January 2019
© Author(s) 2019. CC BY 4.0 License.

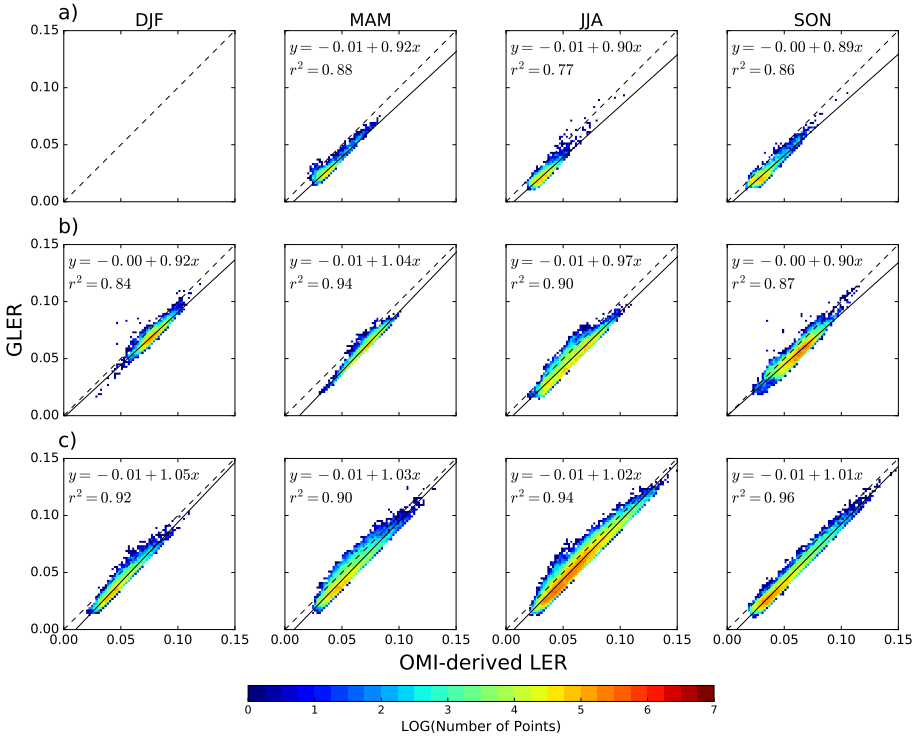

Fig. 6: Comparison of aeorosl and cloud cleared OMI-derived LER at 466 nm and GLER for four seasons of 2006 across a) central Canada; b) central US; and c) Spain/France. In the color-bar legend, N is the number of comparisons.

The GLERs follow a similar seasonal variation as compared with the OMI-derived LER with an absolute difference of 0.01. In the Arabian region the OMI-derived LER and GLER data agree very well because the background aerosols in this high reflectance region have less impact than in other regions due to the brightness of the surface. The Kleipool et al. (2008) LER data (monthly LERs interpolated at 470 nm are used here) exhibit seasonal variations in the various geographic regions but the seasonal variability does not closely follow the OMI-derived LER, possibly because of cloud and/or aerosol contamination. In the winter months, the Kleipool et al. (2008) data agree less well with the OMI-derived LERs, possibly due to the presence of contamination from seasonal snow or clouds in the climatological dataset.

3.3 Interannual variations

When comparing results of calculated GLER against OMI-derived LER, it is important to compare data from multiple years in order to determine whether factors such as land type changes or

Atmos. Meas. Tech. Discuss., https://doi.org/10.5194/amt-2018-327
Manuscript under review for journal Atmos. Meas. Tech.
Discussion started: 8 January 2019
© Author(s) 2019. CC BY 4.0 License.

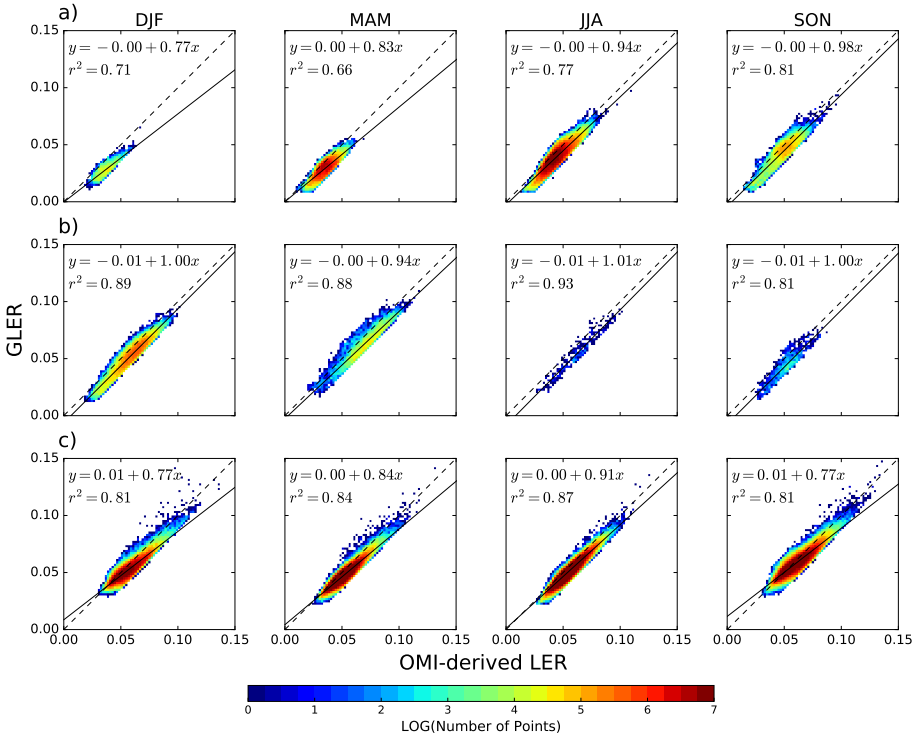

Fig. 7: Similar to Figure 6 but for a) southern Brazil; b) southern India; and c) western Australia.

satellite calibration drifts have an impact. After 2007, OMI radiances in some rows or cross-track positions are affected by an anomaly that occurred outside the instrument, producing a blockage of the intended FOV and/or scattered sunlight from outside the FOV for some rows of the CCD detectors. This is known as the OMI row anomaly, and it affects all wavelengths to some degree (see http://projects.knmi.nl/omi/research/product/rowanomaly-background.php for more information). We therefore limit the year-to-year analysis to rows 1-20 that are not impacted by the row anomaly. We also greatly minimize the impact of snow and ice mis-classification and sub-pixel contamination by restricting our comparison to land surfaces below latitudes of 60°. January and July calculated GLERs are compared with OMI-derived LERs for 2006 and 2015 in Figure 10. Similarly to Figures 6–8, at lower LER values OMI-derived LER is biased slightly high compared with GLER, but for higher LER values GLER and OMI-derived LER are in excellent agreement. There are some outliers where GLER is significantly higher than the OMI-derived LER. This is caused by localized flood plains that appear darker after rain but quickly dry up in a day or two which the MODIS data do not capture this very small scale temporal variability. The good agreement between GLER and OMI-derived LER does not change with season (January vs July) and year (2006 vs 2015), as all

Atmos. Meas. Tech. Discuss., https://doi.org/10.5194/amt-2018-327
Manuscript under review for journal Atmos. Meas. Tech.
Discussion started: 8 January 2019
© Author(s) 2019. CC BY 4.0 License.

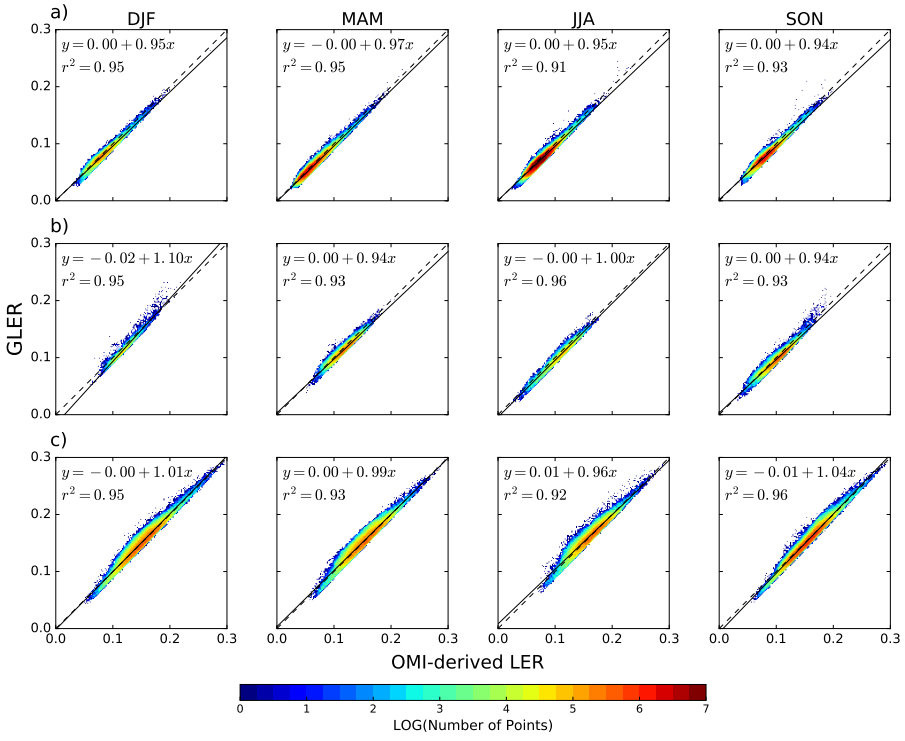

Fig. 8: Similar to Figure 6 but for a) southern Africa; b) Mongolia; and c) Arabian Desert.

plots have identical intercept values and the variability in the slope is at most 0.03.

Figure 11 shows that the mean difference between GLER and OMI-derived LER is smallest for brighter surfaces, whereas the difference gets larger as the surface becomes darker. This agrees with earlier figures and could be caused by higher efficiency of scattering aerosols over darker surfaces than brighter surfaces due to decreased solar radiation being reflected from the darker surface. GLER is smaller than OMI-derived LER because of residual cloud contamination in the OMI data that is not completely screened out. The differences in the July data between 2006 and 2015, though a little bit larger than those in the January data, are still within the calibration uncertainties. Also in July the differences are smaller in 2015 than 2006 until LER reaches 0.20. But given the magnitude of the difference this could be attributed to sampling differences due to aerosol or cloud variability.

3.4 Cross-track dependence

Figure 12 shows LER dependence on the cross-track position across several regions with varying land types. There are two main factors that contribute to the cross-track anisotropy of LER. First and foremost is the BRDF effect. The second factor is the spatial heterogeneity of land coverage within

Atmos. Meas. Tech. Discuss., https://doi.org/10.5194/amt-2018-327
Manuscript under review for journal Atmos. Meas. Tech.
Discussion started: 8 January 2019
© Author(s) 2019. CC BY 4.0 License.

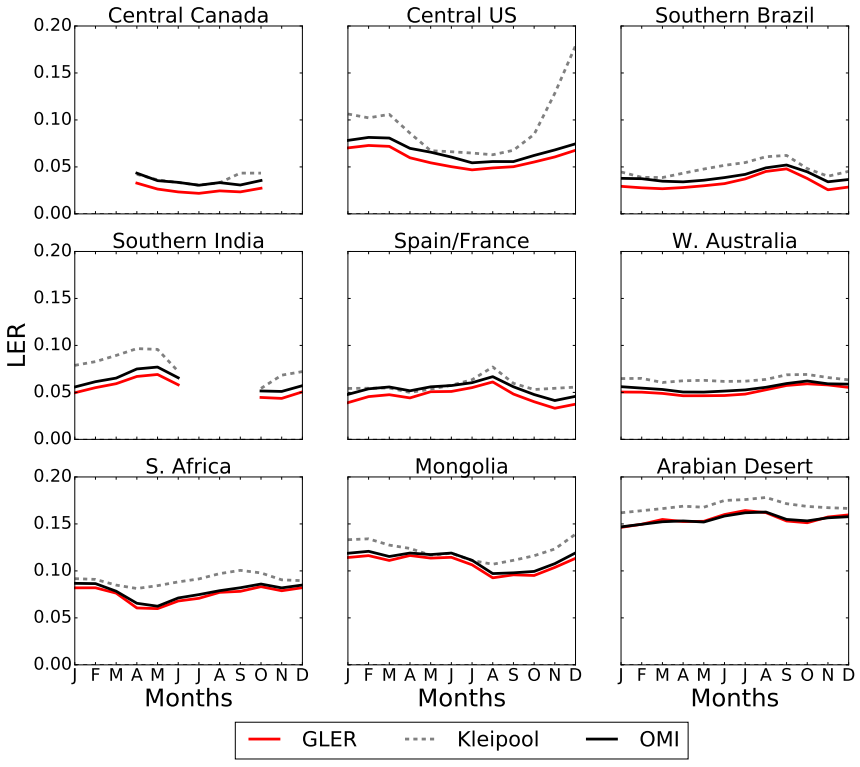

Fig. 9: Seasonal dependence in 2006 of GLER (solid red), Kleipool et al. (2008) climatological LER (dashed), and OMI-derived LER (solid black) at 466 nm.

a selected region (box) that causes a nonuniform distribution of the surface reflectivity. This effect is exaggerated for much larger pixels at the swath edges, as compared with those nearer to the nadir. We try to minimize the second effect by selecting the most uniform regions with sufficient numbers of pixels.

5 However, as one can see from Figure 12, even the Kleipool et al. (2008) climatology, which has no dependence on viewing geometry, shows variations with cross-track position due to spatial nonuniformity of the surface reflectivity for some regions such as Spain/France, Mongolia, and the central US. Due to the BRDF effects, OMI-derived LERs are generally larger further off nadir, in backward scattering directions. The GLER data exhibit a similar dependence, with highest values at
10 the largest VZAs. In several of the brighter regions such as the Arabian desert and western Australia, we note that the GLER is closer to the OMI-derived LER near nadir, with a small bias far off nadir. The darker and more forested regions such as central Canada do not exhibit the same structure in the cross-track dependence.

Atmos. Meas. Tech. Discuss., https://doi.org/10.5194/amt-2018-327
Manuscript under review for journal Atmos. Meas. Tech.
Discussion started: 8 January 2019
© Author(s) 2019. CC BY 4.0 License.

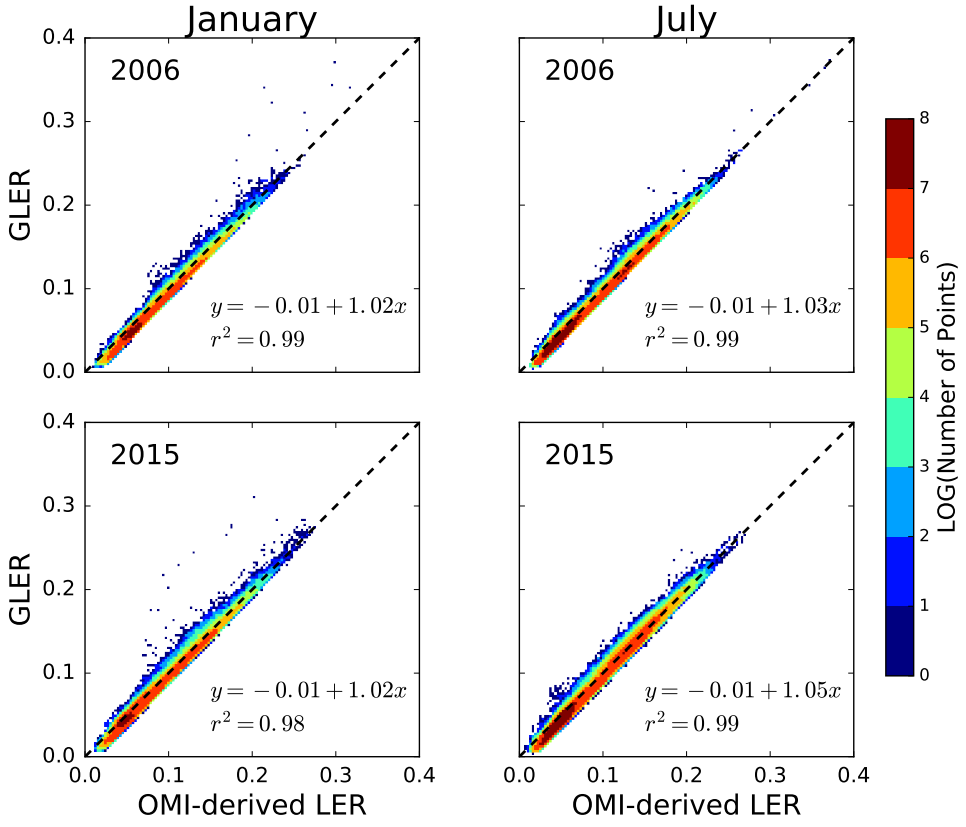

Fig. 10: Scatterplots comparing GLERs with OMI derived LERs at 466 nm in January and July in 2006 and 2015, limited to rows 1-20 to exclude OMI data affected by the row anomaly. Latitudes are restricted to those below 60° to avoid introducing complications of snow/ice mis-classification in the comparison.

3.5 Sub-region case study

To further assess the anisotropy in GLER, we performed a small case study on a sub-region in western Australia (see Figure 13) with very homogeneous land type and elevation. Figure 14b shows that for this sub-region f_{iso}, which is a measure of the surface albedo, is very consistent for all rows due to the homogeneity of the surface. Figure 14a confirms the homogeneity of this region as the Kleipool et al. (2008) climatological LERs are nearly constant for all cross-track positions. We note that $f_{\mathrm{vol}} * k_{\mathrm{vol}}$, which is a measure of the scattering of leaves and background soil/sand particulates in the scene, increases towards the edge of the swath due to increased multiple-scattering. The shadowing effect (i.e., $f_{\mathrm{geo}} * k_{\mathrm{geo}}$) has similar cross-track dependence in backward scattering

Atmos. Meas. Tech. Discuss., https://doi.org/10.5194/amt-2018-327
Manuscript under review for journal Atmos. Meas. Tech.
Discussion started: 8 January 2019
© Author(s) 2019. CC BY 4.0 License.

Atmospheric Measurement Techniques Discussions

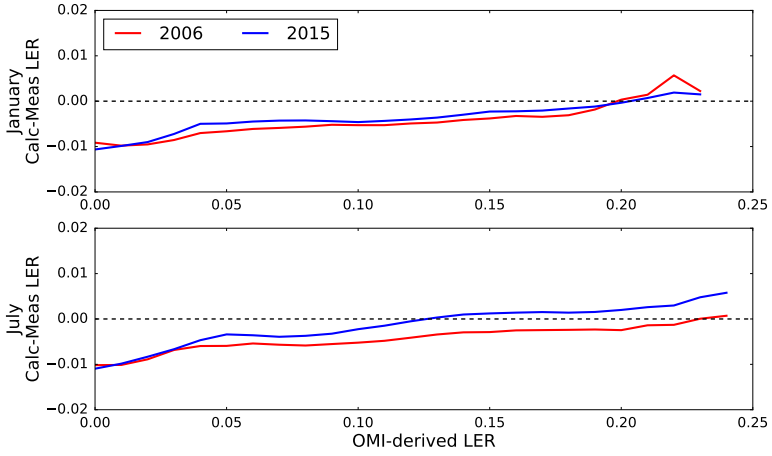

Fig. 11: Differences between calculated GLER and derived OMI LER at 466 nm plotted as a function of OMI derived LER in 2006 and 2015. Data were selected in the same way as those in figure 10.

directions, although somewhat smaller. As seen in Figure 14a, there is a similar pattern in the other regions (Figure 12). In this case study, we note that the bias becomes larger towards the edge of the swath, possibly due to the longer path length allowing for a greater impact from isolated clouds or background aerosols. Nevertheless, the overall cross-track pattern is very similar between the OMI-derived LER and the calculated GLER.

4 Discussion

Vasilkov et al. (2018) reported that values of cloud fractions derived using GLERs in place of climatological LERs are about 0.02 larger on average, and using GLERs can significantly enhance tropospheric NO_2 vertical columns in polluted regions through reduction of the tropospheric air-mass factor (AMF). The results presented in Section 3 are therefore important as they demonstrate that the GLER concept as implemented with MODIS data is able to capture reliably the complex angular, seasonal, and inter-annual variations in OMI reflectances over different regions on the Earth with diverse land cover types.

A significant issue related to the GLER evaluation is the presence of thin clouds and non-absorbing aerosols over land surfaces. Both effectively result in the OMI-retrieved LERs data being larger than the calculated GLERs, since neither was included in the radiative transfer simulations. Here, we excluded data with elevated cloud fractions to mitigate cloud and aerosol effects. However, the fact that OMI-derived LERs are consistently biased high by ∼0.01 relative to GLERs suggests that a certain amount of contamination is unavoidable. In addition to background non-absorbing aerosol and/or residual cloud contamination, this bias may be due to small calibration differences between

Atmos. Meas. Tech. Discuss., https://doi.org/10.5194/amt-2018-327
Manuscript under review for journal Atmos. Meas. Tech.
Discussion started: 8 January 2019
© Author(s) 2019. CC BY 4.0 License.

Atmospheric Measurement Techniques Discussions

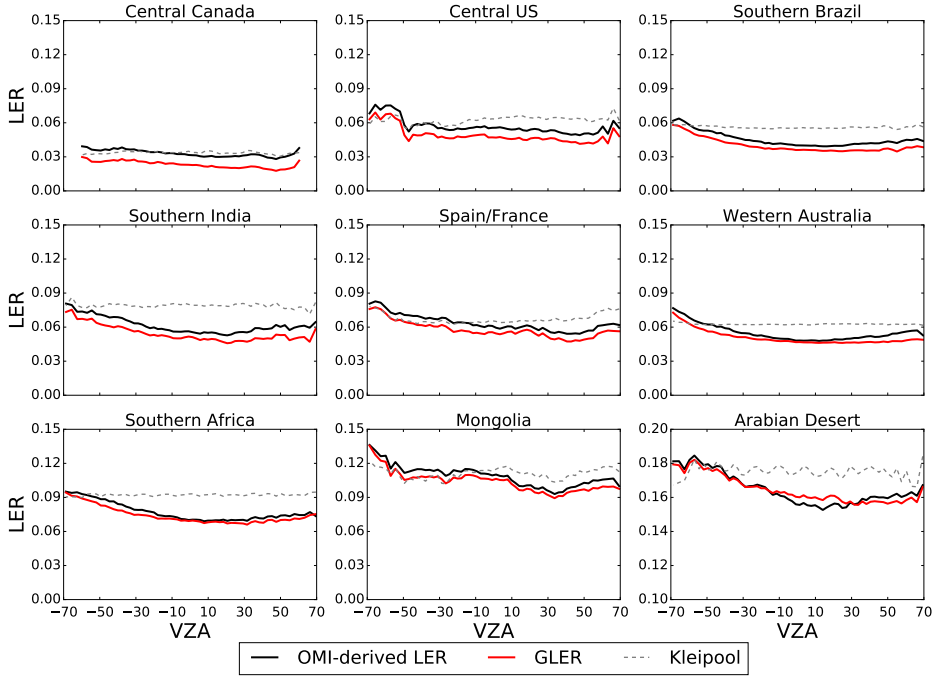

Fig. 12: Cross-track (or VZA) dependence of OMI-derived LER (black line), GLER (red line), and Kleipool et al. (2008) climatological LER (dashed line) for June-August 2006 (December-February 2006 in southern India) across various geographical regions screened for clouds and aerosols. Positive (negative) VZAs denote forward (backward) scattering directions.

MODIS and OMI. Despite all of these factors that introduce some uncertainty into our evaluation, we conclude that the GLER product agrees remarkably well with the OMI measurements in largely clear-sky conditions.

Our results suggest that GLERs may be used with confidence in OMI trace gas retrievals, many of which presently utilize climatological OMI LER data. However, it should also be understood that use of GLERs calculated from aerosol-corrected MODIS BRDF data removes the effects of non-absorbing aerosols that are known to exist in the climatological LER data derived from UV/Vis sensors; this is supported by the slightly elevated OMI-derived LERs we find compared with GLERs. The effects of aerosols are partially accounted for indirectly through the current cloud algorithms that do not distinguish between clouds and non-absorbing aerosol. It is therefore important that the same approach to account of surface effects, whether it be the use of climatological LERs or GLERs, be used for both cloud and trace-gas retrievals.

There are other issues to be considered with the MODIS BRDF model and the Collection 5 gap-filled BRDF parameters (MCD43GF) over seasonal snow cover or permanent ice. The fact that

Atmos. Meas. Tech. Discuss., https://doi.org/10.5194/amt-2018-327
Manuscript under review for journal Atmos. Meas. Tech.
Discussion started: 8 January 2019
© Author(s) 2019. CC BY 4.0 License.

Atmospheric Measurement Techniques Discussions

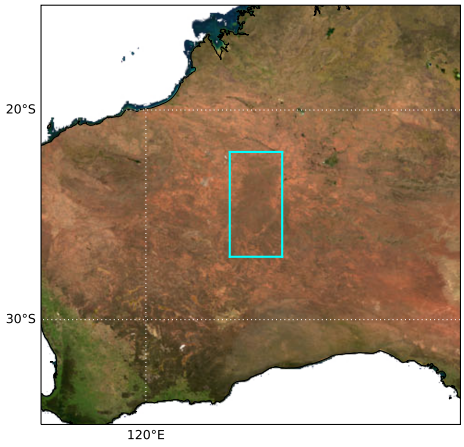

Fig. 13: Map of sub-region in western Australia with homogenous land type used in a case study.

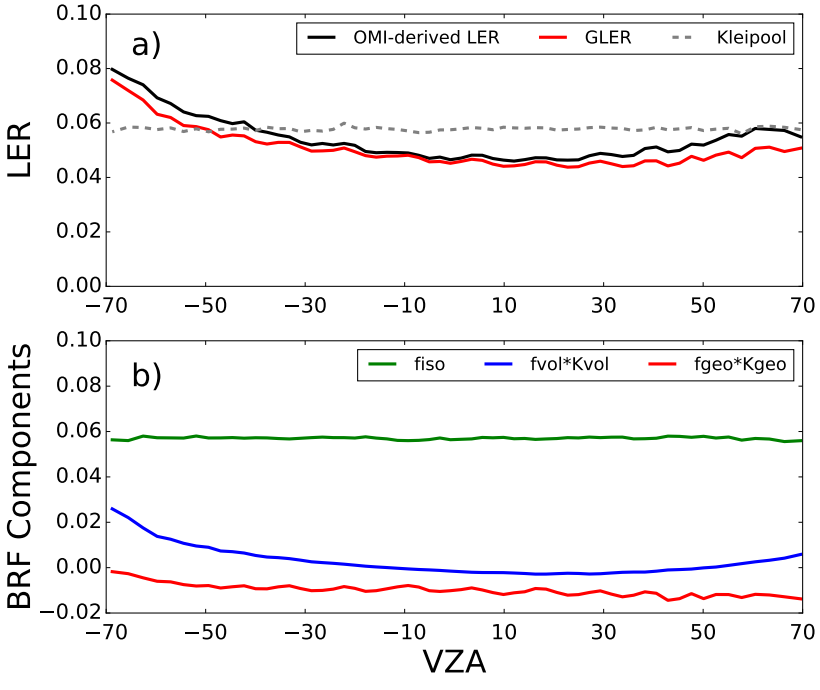

Fig. 14: Case study of cross-track (or VZA) dependence for a sub-region in western Australia in June-August 2006. a) 466 nm LERs; b) BRF components from MODIS data. Positive (negative) VZAs denote forward (backward) scattering directions.

© Author(s) 2019. CC BY 4.0 License.

MCD43GF only provides snow-free land BRDF parameters usually leads to either data gaps or too small GLER values for snow-covered OMI pixels. The current temporary fix to this issue is to use OMI-derived LER but capped by a constant snow albedo of 0.6 as suggested in the KNMI's daily OMI NO_2 (DOMINO) product (Boersma et al., 2011; McLinden et al., 2014) based on the Near-real-time Ice and Snow Extent (NISE) flags (Nolin et al., 2005) in the OMI L1b data set. The second issue is that the current MODIS kernel model lacks a mechanism to deal with strong forward reflection over snow/ice. Finally, since the shortest wavelength in the MODIS BRDF product MCD43GF is 466 nm, it does not cover the shorter range of OMI blue and UV wavelengths. We plan to explore other BRDF products in the future that have more wavelengths and fewer data gaps. A good candidate is the Multi-Angle Implementation of Atmospheric Correction (MAIAC) data (Lyapustin et al., 2012). Compared to MCD43GF, MAIAC includes a shorter wavelength (412 nm) and provides pixel snow fraction that can be used for snow and ice covered regions.

We have focused here on evaluation of land GLERs, because the GLER product is primarily targeted towards improvement of retrievals of trace gas pollutants such as NO_2 that are concentrated over land. We recognize that our evaluation in this paper excludes several important land types, such as compact and dense urban areas, land that is close to water, and a combination of the two. It can be a challenge to collect substantial amounts of data over cities, due to their relatively small size in comparison to the large regions that are the subject of this study. Particulate pollution is also common in urban regions, where non-absorbing sulfate aerosols can interfere with the derivation of LERs, thus making it difficult to validate GLERs with satellite data. These regions require further careful study using data from days when these regions are exceptionally clear. Given the importance of understanding the influence of surface reflectance on AMF calculations in highly polluted regions, we believe this work should be carried out in the future.

The validation results reported in this study apply to OMI and other sensors in similar low-Earth orbits that collect measurements with similar geometries, such as TropOMI, which has higher spatial resolution than OMI (7 km at nadir). In theory, the smaller pixel size of TropOMI and other future sensors should enhance the ability to validate the GLER approach by enabling more complete cloud and aerosol clearing for regions with widespread but broken clouds that were specifically avoided in the present work.

Since MCD43 product is not recommended for solar zenith angles beyond 70° (Schaaf et al., 2011), it may not be applicable for some geostationary (GEO) satellite observations, for which such high solar angles will certainly occur. Instead, GEO instruments such as the Geostationary Operational Environmental Satellite (GOES) imagers may be needed to provide BRDF coefficients that apply to the different range of observing conditions relevant to the planned GEO UV/Vis spectrometers.

Atmos. Meas. Tech. Discuss., https://doi.org/10.5194/amt-2018-327
Manuscript under review for journal Atmos. Meas. Tech.
Discussion started: 8 January 2019
© Author(s) 2019. CC BY 4.0 License.

5 Conclusion

The GLER product has been developed to account for surface BRDF effects on the ultraviolet and visible cloud, trace-gas, and aerosol algorithms. In this paper, we have evaluated the GLER product over land using OMI measurements for a range of land cover types. We described the atmospheric RT and surface BRDF models as well as the sources of data used in those models to produce our GLER product. Over land, the GLER product uses gap-filled Ross-Thick, Li-Sparse kernel BRDF parameters derived from MODIS measurements to capture the directional reflectance properties of the land surface.

We evaluated the GLER product over land by comparing it with OMI-derived LERs over several typical geographical regions focusing on three aspects: seasonal variations, interannual changes, and cross-track dependence. After data are screened to remove the effects of aerosol and cloud contamination, the MODIS-based GLERs show very good agreement with OMI-derived LERs, with correlation coefficients larger than 0.9 for a majority of the selected regions. GLER also captures the seasonal variations and cross-track dependence of the OMI-derived LERs. We attribute a small negative-bias of GLER data relative to OMI LERs in most regions to remaining effects of non-absorbing aerosol and/or cloud contamination and to small differences in MODIS and OMI calibration. Our evaluation has demonstrated that the GLER concept can reliably and efficiently account for surface BRDF effects within UV-Vis cloud and trace-gas retrieval algorithms. In addition, GLERs can be easily incorporated into the existing algorithms.

Appendix A Cox-Munk slope distribution over water surfaces and ancillary input data sets

To characterize scattering anisotropy over water surfaces, we consider light specularly reflected from a rough water surface as well as diffuse light backscattered by water bulk and transmitted through the water surface. We account for polarization at the ocean surface using a full Fresnel reflection matrix as derived by Mishchenko and Travis (1997). We also consider contributions from oceanic foam that can be significant for high wind speeds. Diffuse light from the ocean is described by a Case 1 water model that has chlorophyll concentration as a single input parameter (Morel, 1988). Our Case 1 water model accounts for the anisotropic nature of light backscattered by the ocean (Morel and Gentili, 1996).

Details regarding the ancillary data sets used for water GLER calculation are provided in Table 3. Pixel chlorophyll concentration is needed to calculate the water-leaving radiance contribution; wind speed and direction are essential input parameters for sunglint intensity calculation. Here, a $2.5'$ monthly climatology of chlorophyll-a concentration derived with Aqua MODIS Ocean Color Chlorophyll (OCI) algorithm (https://oceancolor.gsfc.nasa.gov/atbd/chlor_a/) is selected - this dataset has excellent cloud screening and calibration as compared with other sensors including Terra MODIS. We use sea-surface wind speed retrieval from the Advanced Microwave Scanning Radiome-

Atmos. Meas. Tech. Discuss., https://doi.org/10.5194/amt-2018-327
Manuscript under review for journal Atmos. Meas. Tech.
Discussion started: 8 January 2019
© Author(s) 2019. CC BY 4.0 License.

ter for EOS (AMSR-E) on board Aqua, which is followed closely by the Aura platform (with OMI). AMSR-E has high spatial resolution ($0.25°$) grids (Wentz and Meissner, 2004). 2-D interpolation is applied to obtain the averaged wind speed over an OMI pixel FOV. Since AMSR-E is not available after October 2011, we switch to the first Special Sensor Microwave Imager/Sounder (SSMIS) F16 satellite (launched in Oct, 2003) data (F16 SSMIS). The SSMIS-derived wind speed has the same spatial resolution as AMSR-E (https://ghrc.nsstc.nasa.gov/hydro/details/rssmif16d). Wind direction is specified from NASA Global Modeling and Assimilation Office (GMAO) Forward Processing for Instrument Teams (FP-IT) data ($0.625° \times 0.5°$ grids at every one hour, see GMAO at https://gmao.gsfc.nasa.gov/GMAO_products/ for more information). For those ancillary data that have coarser spatial but higher temporal resolutions than those of OMI itself, such as the wind direction dataset, a 2-D collocation (time and space) and interpolation is applied to obtain the average over the OMI FOV.

Table 3: Spatial and temporal resolutions of ancillary data used for water GLER calculation

Name	Source	Spatial	Temporal
Chlorophyll-a concentration	MODIS Aqua	$2.5'$	monthly
Wind speed (before Oct 2011)	AMSR-E/Aqua	$0.25°$	N/A
Wind speed (after Oct 2011)	SSMIS/F16	$0.25°$	N/A
Wind direction	FP-IT/GMAO	$0.625° \times 0.5°$	1 hour

Appendix B Pixel averaged terrain height and pressure

In order to estimate the pixel-based surface pressure, a critical input parameter to the air mass factor in the NO_2 algorithm as well as to total optical depth of the Rayleigh atmosphere, terrain height derived from high resolution DEM data averaged over OMI pixel FOV is required. In the GLER product, we derived pixel average terrain height from surface topographic data (ETOPO2v2), $2'$ gridded global relief data with the vertical precision of 1 m from the NOAA National Centers for Environmental Information (NCEI) Marine Geology and Geophysics (https://www.ngdc.noaa.gov/mgg/global/etopo2.html), in which positive values represent altitude above sea level while negative values represent depth below sea level. To derive the correct terrain height, we need first to determine the surface type for each ETOPO2v2 cell. This can be done by preprocessing the ETOPO2v2 data with the $30''$ MODIS land-water flag map described in Section 2.1. If the cell's surface type is land or inland water, we keep both positive and negative values; if it is ocean, we zero out negative values. Then we average the preprocessed ETOPO2v2 data within the OMI FOV. This approach produces a less noisy result for terrain height than the original OMI L1b terrain height which is the value at the center of the pixel (see Figure 15).

Atmos. Meas. Tech. Discuss., https://doi.org/10.5194/amt-2018-327
Manuscript under review for journal Atmos. Meas. Tech.
Discussion started: 8 January 2019
© Author(s) 2019. CC BY 4.0 License.

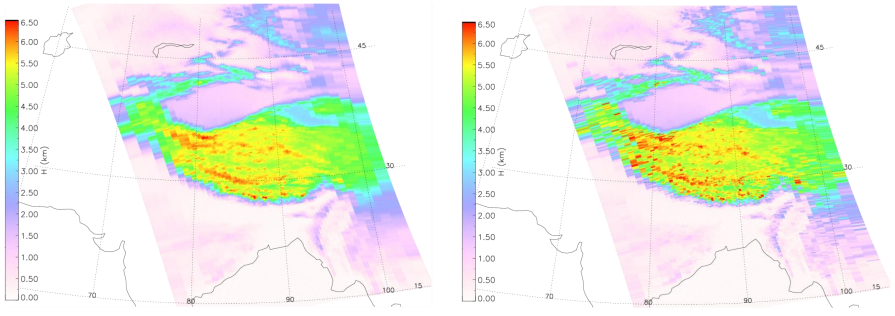

Fig. 15: Pixel average terrain height for region of the Tibetan plateau from ETOPO2v2 used in GLER (left), and OMI L1b terrain height at the center of the pixel (right).

Given the pixel average terrain height (z), the terrain pressure (P_s) for the OMI pixel is calculated as

$$P_s = P_s(\mathrm{GMI}) \exp\Big(-\frac{z - z(\mathrm{GMI})}{H}\Big), \tag{B1}$$

$$H = (kT)/(Mg) \tag{B2}$$

where $P_s(\mathrm{GMI})$ is the surface pressure monthly climatology (1° latitude by 1.25° longitude spatial resolution) taken from the Global Modeling Initiative (GMI) chemistry transport model driven by fields from the NASA GMAO Goddard Earth Observing System 5 (GEOS-5) global data assimilation system (Rienecker et al., 2011), $z(\mathrm{GMI})$ is the terrain height at the GMI resolution of $1° \times 1.25°$, k is Boltzmann constant, T is the GMI air temperature at the surface, M is the mean molecular weight of air, and g is the acceleration due to gravity.

Appendix C Look-up tables

From an operational point of view, it is impractical to process OMI and similar satellite data with online radiative transfer calculations. For example, for OMI there are more than 14 years of global data, and there will be a much larger data turn-round for the recently launched TROPOspheric Monitoring Instrument (TropOMI) and the upcoming TEMPO mission (Tropospheric Emissions: Monitoring of Pollution). Since our goal is to create a global GLER product for generic satellite missions, a look-up-table (LUT) approach is adopted to calculate variables in Eq. 2 such as I_{comp}, I_0, T and S_b (see Table 4 for details). These LUTs have sufficient nodes to cover all possible OMI geometries (SZA, VZA and RAA) and model input parameters, such as three surface BRDF kernel coefficients (f_{iso}, f_{vol}, and f_{geo}) for land and chlorophyll concentration, wind speed and direction for waters at different surface pressure levels. The LUT approach has been validated with online VLIDORT

© Author(s) 2019. CC BY 4.0 License.

calculations; this shows a satisfactory results of better than 0.5% relative differences between online calculations and interpolated TOA radiances.

Table 4: LUT structures for input parameters

Parameter	Number of nodes	Step(s)	Range
Pressure	11	20-110	411-1100 hPa
SZA	45	2	0-86°
VZA	41	2	0-80°
RAA	48	2-5	0-180°
f_{iso}	25	0.01-0.04	0.01-0.999
f_{vol}	16	0.01-0.1	0-0.5
f_{geo}	12	0.005-0.02	0-0.1
Chlorophyll	24	0.003-3.0	0.01-10 $\mathrm{mg/m^3}$
Wind speed	23	0.2-5.0	0.001-50 $\mathrm{m/s}$
Wind direction	36	10	0-360°

Author contributions. WQ wrote the manuscript, developed the GLER algorithm and created the GLER product. ZF computed OMI-derived LER and analyzed the comparison results. DH supported the GLER development and contributed writing Sect 2.2 and Sect 4. AV proposed the GLER concept and supported implementation of the algorithm. JJ supported the GLER development and provided a general framework of the manuscript. NK proposed the GLER concept and supported the GLER development. BF provided coding support for MODIS-OMI pixel collocation. RS developed the VLIDORT code needed for computation of radiance LUTs.

Competing interests. The authors declare that they have no conflict of interest.

Acknowledgements. Funding for this work was provided by NASA through Aura core team funding as well as the Aura project and Aura Science Team and Atmospheric Composition Modeling and Analysis Program managed by Kenneth Jucks and Barry Lefer. We acknowledge Crystal Schaaf for providing gap-filled MODIS MCD43GF BRDF data, and the MODIS data processing team as well as the OMI calibration team at KNMI and NASA. We thank Alexei Lyapustin and Crystal Schaaf for helpful discussions.

© Author(s) 2019. CC BY 4.0 License.

References

Boersma, K. F., Eskes, H. J., Dirksen, R. J., van der A, R. J., Veefkind, J. P., Stammes, P., Huijnen, V., Kleipool, Q. L., Sneep, M., Claas, J., Leitão J., Richter, A., Zhou, Y., and Brunner, D.: An improved tropospheric NO_2 column retrieval algorithm for the Ozone Monitoring Instrument, Atmos. Meas. Tech., 4, 1905–1928, doi:10.5194/amt-4-1905-2011, 2011.

Bodhaine, B. A., Wood, N. B., Dutton, E. G., and Slusser, J. R.: On Rayleigh Optical Depth Calculations, J. Atmos. Ocean. Tech., 16: 1854–1861, doi:10.1175/1520-0426,1999.

Cox, C. and Munk, W.: Statistics of the sea surface derived from sun glitter, J. Mar. Res. 13, 198–227, 1954.

Dave, J. V.: Effect of aerosol on the estimation of total ozone in an atmospheric column from the measurements of the ultraviolet radiance, J. Atmos. Sci., 35, 899–911, 1978.

Dobber, M., Q. Kleipool, R. Dirksen, P. Levelt, G. Jaross, S. Taylor, T. Kelly, L. Flynn, G. Leppelmeier, and Rozemeijer, N.: Validation of Ozone Monitoring Instrument level 1b data products, J. Geophys. Res., 113, D15S06, doi:10.1029/2007JD008665, 2008.

Fisher, B., Joiner, J., Vasilkov, A., Veefkind, P., Platnick, S., and Wind, G.: A New A-train Cloud Product that Co-locates OMI and MODIS Cloud and Radiance Parameters onto the OMI Footprint. EOS Aura Science Team Meeting, College Park, MD United States, 2014. Available at https://ntrs.nasa.gov/search.jsp/?R=20150001342.

Franch, B., Vermote, E. F., Sobrino, J. A., and Fedele, E.: Analysis of directional effects on atmospheric correction, Remote Sens. Env., 128, 276–288, 2013.

Haines, E.,: Point in Polygon Strategies, Graphics Gems IV, ed. Paul Heckbert, Academic Press, pp. 24–46, 1994.

Herman, J. R. and Celarier, E.: Earth surface reflectivity climatology at 340 to 380 nm from TOMS data, J. Geophys. Res., 102, 28003–28011, 1997.

Jaross, G., and J. Warner, J.: Use of Antarctica for validating reflected solar radiation measured by satellite sensors, J. Geophys. Res., 113, D16S34, doi:10.1029/2007JD008835, 2008.

Justice, C. O., Vermote, E., Townshend, J. R. G., Defries, R., Roy, D. P., Hall, D. K., Salomonson, V. V., Privette, J. L., Riggs, G., Strahler, A., Lucht, W., Myneni, R. B., Lewis, P., and Barnsley, M. J.: The Moderate Resolution Imaging Spectroradiometer (MODIS): Land remote sensing for global change research, IEEE Trans. Geosci. Remote Sens., 36, 1228-1249, 1998.

Kay, S. J. D., Hedley, and Lavender, S.: Sun glint correction of high and low spatial resolution images of aquatic scenes: a review of methods for visible and near-Infrared wavelengths, Remote Sensing, 1, 697–730, doi:10.3390/rs1040697, 2009.

Kleipool, Q. L., Dobber, M. R., de Haan, J. F., and Levelt, P. F.: Earth surface reflectance climatology from 3 years of OMI data, J. Geophys. Res., 113, D18308, doi:10.1029/2008jd010290, 2008.

Knobelspiesse, K. D., Cairns, B., Schmid, B., Roman, M. O., and Schaaf, C. B.: Surface BRDF estimation from an aircraft compared to MODIS and ground estimates at the Southern Great Plains site, J. Geophys. Res., 113, D20105, doi:10.1029/2008JD010062, 2008.

Koelemeijer, R. B. A., Stammes, P., Hovenier, J. W., and de Haan, J. F.: A fast method for retrieval of cloud parameters using oxygen A-band measurements from the Global Ozone Monitoring Experiment, J. Geophys. Res., 106, 3475–3496, 2001.

© Author(s) 2019. CC BY 4.0 License.

Kotchenova, S. Y., and Vermote, E. F.: Validation of a vector version of the 6S radiative transfer code for atmospheric correction of satellite data. Part II: Homogeneous Lambertian and anisotropic surfaces, Appl. Opt., 46(20), 4455–4464, doi:10.1364/AO.46.004455, 2007.

Krotkov, N. A., Lamsal, L. N., Celarier, E. A., Swartz, W. H., Marchenko, S. V., Bucsela, E. J., Chan, K. L., Wenig, M., and Zara, M.: The version 3 OMI NO_2 standard product, Atmos. Meas. Tech., 10, 3133-3149, https://doi.org/10.5194/amt-10-3133-2017, 2017.

Lamsal, L. N., Krotkov, N. A., Celarier, E. A., Swartz, W. H., Pickering, K. E., Bucsela, E. J., Gleason, J. F., Martin, R. V., Philip, S., Irie, H., Cede, A., Herman, J., Weinheimer, A., Szykman, J. J., and Knepp, T. N.: Evaluation of OMI operational standard NO_2 column retrievals using in situ and surface-based NO_2 observations, Atmos. Chem. Phys., 14, 11587-11609, doi:10.5194/acp-14-11587-2014, 2014.

Li, X., Strahler, A.H.: Geometric-optical bidirectional reflectance modeling of the discrete crown vegetation canopy: effect of crown shape and mutual shadowing, IEEE Trans. Geosci. Remote Sens., 30, 276–292,1992.

Liu, J., Schaaf, C., Strahler, A., Jiao, Z., Shuai, Y., Zhang, Q., Roman, M., Augustine, J. A., and Dutton, E. G.: Validation of Moderate Resolution Imaging Spectroradiometer (MODIS) albedo retrieval algorithm: Dependence of albedo on solar zenith angle, J. Geophys. Res., 114, D01106, doi:10.1029/2008JD009969, 2009.

Lorente, A., Boersma K. F., Stammes, P., Tilstra, L. G., Richter, A., Yu, H., Kharbouche, S., and Muller, Jan-Peter: The importance of surface reflectance anisotropy for cloud and NO_2 retrievals from GOME-2 and OMI, Atmos. Meas. Tech., 11, 4509-4529, https://doi.org/10.5194/amt-11-4509-2018, 2018.

Lucht, W., Schaaf, C. B., and Strahler, A. H.: An algorithm for the retrieval of albedo from space using semiempirical BRDF models, IEEE T. Geosci. Remote Sens., 38, 977–998, 2000.

Lyapustin, A., Wang, Y., Laszlo, I., Hilker, T., Hall, F., Sellers, P., Tucker, J., Korkin, S.: Multi-angle implementation of atmospheric correction for MODIS (MAIAC). 3: Atmospheric correction, Rem. Sens. Environ., http://dx.doi.org/10.1016/j.rse.2012.09.002, 2012.

Martonchik, J. V., Bruegge, C. J., and Strahler, A. H.: A review of reflectance nomenclature used in remote sensing, Remote Sens. Reviews, 19, 9–20, 2000.

McLinden, C. A., Fioletov, V., Boersma, K. F., Kharol, S. K., Krotkov, N., Lamsal, L., Makar, P. A., Martin, R. V., Veefkind, J. P., and Yang, K.: Improved satellite retrievals of NO_2 and SO_2 over the Canadian oil sands and comparisons with surface measurements, Atmos. Chem. Phys., 14, 3637–3656, doi:10.5194/acp-14-3637-2014, 2014.

Mishchenko, M. I. and Travis, L. D.: Satellite retrieval of aerosol properties over the ocean using polarization as well as intensity of reflected sunlight, J. Geophys. Res., 102, 16989–17013, doi:10.1029/96JD02425, 1997.

Morel, A.: Optical modeling of the upper ocean in relation to its biogeneous matter content (Case I waters), J. Geophys. Res., 93, 10749–10768, 1988.

Morel, A. and Gentili, B.: Didduse reflectance of oceanic water. III. Implication of bidirectionality for the remote-sensing probe, Appl. Opt., 35, 4850–4862, 1996.

Nolin, A., Armstrong, R., and Maslanik, J.: Near real-time SSM/I EASE-grid daily global ice concentration and snow extent, Digit. Media, Natl. Snow Ice Data Center, Boulder, CO, USA, 2005.

Noguchi, K., Richter, A., Rozanov, V., Rozanov, A., Burrows, J. P., Irie, H., and Kita, K.: Effect of surface BRDF of various land cover types on geostationary observations of tropospheric NO_2, Atmos. Meas. Tech.,

© Author(s) 2019. CC BY 4.0 License.

7, 3497-3508, doi:10.5194/amt-7-3497-2014, 2014.

Nicodemus, F.: Directional reflectance and emissivity of an opaque surface, Appl. Opt., 4, 767-775, 1965.

Nicodemus, F. E., et al. (1977). Geometrical considerations and nomenclature for reflectance. Washington, DC: National Bureau of Standards, US Department of Commerce. URL: http://physics.nist.gov/Divisions/Div844/ facilities/specphoto/pdf/geoConsid.pdf

Qin, W., Goel, N. S., and Wang, B.: The hotspot effect in heterogeneous vegetation canopies and performances of various hotspot models, Remote Sens. Reviews, 14, 283–332, 1996.

Rienecker, M. M., Suarez, M. J., Gelaro, R., Todling, R., Bacmeister, J., Liu, E., Bosilovich, M. G., Schubert, S. D., Takacs, L., Kim, G.-K., Bloom, S., Chen, J., Collins, D., Conaty, A., da Silva, A., Gu, W., Joiner, J., Koster, R. D., Lucchesi, R., Molod, A., Owens, T., Pawson, S., Pegion, P., Redder, C. R., Reichle, R., Robertson, F. R., Ruddick, A. G., Sienkiewicz, M., and Woollen, J.: MERRA: NASA′s Modern-Era Retrospective Analysis for Research and Applications, J. Climate, 24, 3624–3648, doi:10.1175/JCLI-D-11-00015.1, 2011.

Rencz, A. N., and R. A. Ryerson (Editors), 1999, Manual of Remote Sensing, Volume 3, Remote Sensing for the Earth Sciences, 3rd Edition BOOK, ISBN: 978-0-471-29405-4, Wiley, 1999.

Riggs, G.A., D.K. Hall, and M.O. Romn, 2016. MODIS Snow Products Collection 6 User Guide, NASA MODIS project document.

Roman, M. O., Schaaf, C. B., Woodcock, C. E., Strahler, A. H., Yang, X., Braswell, R. H., Curtis, P. S., Davis, K. J., Dragoni, D., Goulden, M. L., Gu, L., Hollinger, D. Y., Kolb, T. E., Meyers, T. P., Munger, J. W., Privette, J. L., Richardson, A. D., Wilson, T. B., and Wofsy, S. C.: The MODIS (Collection V005) BRDF/albedo product: Assessment of spatial representativeness over forested landscapes, Remote Sens. Env., 113, 2476-2498, 2009.

Roman, M. O., Gatebe, C. K., Shuai, Y., Wang, Z., Gao, F., Masek, J. G., He, T., Liang, S., and Schaaf, C. B.: Use of in situ and airborne multiangle data to assess MODIS- and Landsat-based estimates of directional feflectance and albedo, IEEE Trans. Geosci. Remote Sens., 51, 1393-1403, 2013.

Roujean, J., Leroy, M., Deschamps, P. A bidirectional reflectance model of the Earths surface for the correction of remote sensing data, J. Geophys. Res., 97, 20455–20468, 1992.

Ross, J. V, The Radiation Regime and Architecture of Plant Stands 3. BOOK, Springer Science & Business Media, 1981.

Salomon, J. G., Schaaf, C. B., Strahler, A. H., Gao, F., and Jin Y.: Validation of the MODIS bidirectional reflectance distribution function and albedo retrievals using combined observations from the Aqua and Terra platforms, IEEE Trans. Geosci. Remote Sens., 44, 1555-1565, 2006.

Schaaf, C. B., Gao, F., Strahler, A. H., Lucht, W., Li, X., Tsang, T., Strugnell, N. C., Zhang, X., Jin, Y., Muller, J.-P., Lewis, P., Barnsley, M., Hobson, P., Disney, M., Roberts, G., Dunderdale, M., Doll, C., d'Entremont, R., Hu, B., Liang, S., and Privette, J. L.: First operational BRDF, albedo and nadir reflectance products from MODIS, Remote Sens. Environ., 83, 135–148, 2002.

Schaaf, C. L. B., Liu, J., Gao, F., and Strahler, A. H.: MODIS albedo and reflectance anisotropy products from Aqua and Terra, In Land Remote Sensing and Global Environmental Change: NASA's Earth Observing System and the Science of ASTER and MODIS, Remote Sensing and Digital Image Processing Series, Vol.11, B. Ramachandran, C. Justice, M. Abrams, Eds, Springer-Verlag, 873 pp., 2011.

© Author(s) 2019. CC BY 4.0 License.

Schaepman-Strub, G., Schaepman, M. E., Painter, T. H., Dangel, S., Martonchik, J. V., Reflectance quantities in optical remote sensing–definitions and case studies, Remote Sens. Environ., 103, 27–42, 2006.

Schenkeveld, V. M. E., Jaross, G., Marchenko, S., Haffner, D., Kleipool, Q. L., Rozemeijer, N. C., Veefkind, J. P., and Levelt, P. F.: In-flight performance of the Ozone Monitoring Instrument, Atmos. Meas. Tech., 10, 1957–1986, doi:10.5194/amt-10-1957-2017, 2017.

Sobrino, J.A., Franch, B., Oltra-Carri, R., Vermote, E. F., and Fedele, E,: Evaluation of the MODIS Albedo product over a heterogeneous agricultural area, Int. J. Remote Sensing, 34, 5530–5540, 2013.

Spurr, R. J. D.: VLIDORT: a linearized pseudo-spherical vector discrete ordinate radiative transfer code for forward model and retrieval studies in multilayer multiple scattering media, J. Quant. Spectr. Rad. Trans., 102, 316–421, 2006.

Sun, Q., Wang, Z., Li, Z., Erb, A., and Schaaf, C. B.: Evaluation of the global MODIS 30 arc-second spatially and temporally complete snow-free land surface albedo and reflectance anisotropy dataset, Intl. J. Appl. Earth Obs. Geoinfo., 58, 36–49, doi:10.1016/j.jag-01-011-2017, 2017.

Torres, O., Tanskanen, A., Veihelman, B., Ahn, C., Braak, R., Bhartia, P. K., Veefkind, V., and Levelt, P.: Aerosols and Surface UV Products from OMI Observations: An Overview, J. Geophys. Res., 112, D24S47, doi:10.1029/2007JD008809, 2007.

Vasilkov, A. P., Qin, W., Krotkov, N., Lamsal, L., Spurr, R., Haffner, D., Joiner, J., Yang, E.-S., and Marchenko, S., Accounting for the effects of surface BRDF on satellite cloud and trace-gas retrievals: a new approach based on geometry-dependent Lambertian equivalent reflectivity applied to OMI algorithms, Atmos. Meas. Tech., 10, 333–349, doi:10.5194/amt-10-333-2017, 2017.

Vasilkov, A. P., Yang, E.-S., Marchenko, S., Qin, W., Lamsal, L., Joiner, J., Krotkov, N., Bhartia, P. K. and Spurr, R.: A cloud algorithm based on the O_2-O_2 477 nm absorption band featuring an advanced spectral fitting method and the use of surface geometry-dependent Lambertian-equivalent reflectivity, Atmos. Meas. Tech., 11, 4093–4107, doi:10.5194/amt-11-4093-2018, 2018.

Veefkind, J. P., de Haan, J. F., Sneep, M., and Levelt, P. F.: Improvements to the OMI (O_2-O_2) operational cloud algorithm and comparisons with ground-based radar-lidar observations, Atmos. Meas. Tech., 9, 6035–6049, doi:10.5194/amt-9-6035-2016, 2016.

Vermote, E.F., Tanre, D., Deuze, J. L., Herman, M., Morcrette, J. J.: Second Simulation of the Satellite Signal in the Solar Spectrum: an overview, IEEE Trans. Geosci. Remote Sens., 35, 675-686, 1997.

Vermote, E. F., El Saleous, N. Z., Justice, C. O.: Atmospheric correction of MODIS data in the visible to middle infrared: first results, Remote Sens. Env., 83, 97–111, 2002.

Vermote, E. F., and Kotchenova, S.: Atmospheric correction for the monitoring of land surfaces, J. Geophys. Res., 113, D23S90, doi:10.1029/2007JD009662, 2008.

Wang, K., Liang, S., Schaaf, C. L., and Strahler, A. H.: Evaluation of Moderate Resolution Imaging Spectro-radiometer land surface visible and shortwave albedo products at FLUXNET sites, J. Geophys. Res., 115, D17107, doi:10.1029/2009JD013101, 2010.

Wang, P., Stammes, P., van der A, R., Pinardi, G., and van Roozendael, M.: FRESCO+: an improved O_2 A-band cloud retrieval algorithm for tropospheric trace gas retrievals, Atmos. Chem. Phys., 8, 6565–6576, doi:10.5194/acp-8-6565-2008, 2008.

Wang, Z, Schaaf, C. B., Sun, Q., Shuai, Y., and Romn, M. O., Capturing rapid land surface dynamics

© Author(s) 2019. CC BY 4.0 License.

with Collection V006 MODIS BRDF/NBAR/Albedo (MCD43) products, Remote Sens. Env., 207, 50-64, https://doi.org/10.1016/j.rse.2018.02.001, 2018.

Wentz, F. J., Meissner T.: AMSR-E/Aqua L2B Global Swath Ocean Products Derived from Wentz Algorithm V002 (January 2009, June to August 2010). Updated daily. Boulder, Colorado USA: National Snow and Ice Data Center. Digital media, 2004.

Yang, E.-S., Vasilkov, A., Joiner, J., Marchenko, S., Krotkov, N., Haffner, D., and Bhartia, P. K.: A new cloud pressure algorithm based on the (O_2-O_2) absorption band at 477 nm, OMI Science Team Meeting, de Bilt, Netherlands, 2015. Available at http://projects.knmi.nl/omi/research/project/meetings/ostm19/pres_ostm19_20150831.php.

Zhou, Y., Brunner, D., Spurr, R. J. D., Boersma, K. F., Sneep, M., Popp, C., and Buchmann, B.: Accounting for surface reflectance anisotropy in satellite retrievals of tropospheric NO_2, Atmos. Meas. Tech., 3, 1185–1203, doi:10.5194/amt-3-1185-2010, 2010.